Reconstructing Free-Flight Angular Velocity from a Miniaturized Wireless Accelerometer

Ryan McGinnis
Graduate Student
Member ASME
e-mail: ryanmcg@umich.edu

N. C. Perkins
Fellow ASME

Kevin King
Postdoctoral Researcher

Mechanical Engineering,
University of Michigan,
Ann Arbor, MI 48109-2125

The theory governing the torque-free motion of a rigid body is well established, yet direct experimental measurement in the laboratory remains an obvious challenge. This paper addresses this challenge by presenting a novel miniature wireless inertial measurement unit (IMU) that directly measures the motion of a rigid body during free-flight. The IMU incorporates three-axis sensing of acceleration and three-axis sensing of angular velocity with a microcontroller and an RF transceiver for wireless data transmission to a host computer. Experiments consider a rigid body that is spun up by hand and then released into free-flight. The measured rotational dynamics from the IMU are carefully benchmarked against theoretical predictions. This benchmarking reveals that the angular velocity directly measured by the angular rate gyros lies within 6% of that predicted by the (Jacobi elliptic function) solutions to the Euler equations. Moreover, experimentally constructed polhodes elegantly illustrate the expected stable precession for rotations initiated close to the major or minor principal axes and the unstable precession for rotations initiated close to the intermediate axis. We then present a "gyro-free" design that employs a single, triaxial accelerometer to reconstruct the angular velocity during free-flight. A measurement theory is presented and validated experimentally. Results confirm that the angular velocity can be reconstructed with exceedingly small errors (less than 2%) when benchmarked against direct measurements using angular rate gyros. The simpler gyro-free design addresses restrictions imposed by rate gyro cost, size, and measurement range and may enable high-volume commercial applications of this technology in instrumented baseballs, basketballs, golf balls, footballs, soccer balls, softballs, and the like. [DOI: 10.1115/1.4006162]

1 Introduction

The theory governing the torque-free motion of a rigid body is a classical topic in rigid body dynamics; see for example, [1–3]. Under torque-free conditions, the solution to Euler's equations for the angular velocity, expressible by Jacobi elliptic functions, satisfies two first integrals; namely constant rotational kinetic energy and constant magnitude of angular momentum. Rotations initiated close to the major or the minor principal axis generates a stable periodic precession about those axes. By contrast, unstable precession results from rotations initiated close to the intermediate axis. These results are elegantly revealed using the geometrical construction due to Poinsot [1–4], which considers the rolling without slipping of the inertia ellipsoid on the invariable plane. The path traced on the inertia ellipsoid by its contact point on the invariant plane, referred to as the polhode, describes the precession of the angular velocity vector in a body-fixed frame. The polhode may also be constructed from the intersection of the rotational kinetic energy ellipsoid and the angular momentum ellipsoid in angular velocity space [5]. This latter method will be demonstrated experimentally later in this paper.

In contrast to the well-established theory, direct experimental measurements of the dynamics of rigid bodies during torque-free or "free-flight" motion remain scarce. This is not surprising given the significant experimental challenges in measuring free-flight dynamics in the laboratory in a noninvasive manner. One means to accomplish this is through camera-based motion analysis as used; for example, in optical motion tracking; see [6–13]. Bhat et al. [12] deduce the motion of a rigid body using single-camera optical motion tracking paired with global optimization techniques to minimize the error between video- and simulation-derived silhouettes. The algorithm, designed to converge to optimum values for initial position, orientation, velocity, and angular velocity, is especially sensitive to initial guesses due to many local minima in the error space. A variant of camera-based measurement introduced by Masutani et al. [13] estimates the free rotational motion of a rigid body from a sequence of grayscale or distance images. This method, which relies heavily on the aforementioned closed-form solutions to Euler's equations, was evaluated using simulated motions in lieu of experiments. Fundamentally, camera-based motion analysis begins with noisy position data that must be differentiated numerous times to yield velocity, angular velocity, acceleration, and angular acceleration data for the purpose of comparing with the equations of rigid body motion. The successive differentiation of real (i.e., noisy) position data leads to noise amplification and yields potentially error-prone comparisons with theory. Additionally, to avoid problems with aliasing, a camera must also capture images (and without occlusions) at frame rates well in excess of the angular velocity of the rigid body. These challenges fundamentally limit the utility of camera-based methods for analyzing the dynamics of a rigid body.

The use of MEMS inertial sensors to directly measure rigid body dynamics presents an attractive alternative to camera-based motion detection. Inertial sensors, consisting of accelerometers and angular rate gyros, directly measure the kinematic quantities governed by the Newton-Euler differential equations of motion. As one example, Lorenz [14] investigated the flight and attitude dynamics of a Frisbee ™ using a body-fixed instrumentation package containing two dual-axis MEMS accelerometers (among other sensors) to deduce the aerodynamic coefficients of the disk.

Contributed by the Applied Mechanics of ASME for publication in the JOURNAL OF APPLIED MECHANICS. Manuscript received June 25, 2010; final manuscript received February 16, 2012; accepted manuscript posted February 23, 2012; published online May 11, 2012. Assoc. Editor: Wei-Chau Xie.

Of keen interest in free-flight dynamics is the rotation of the rigid body as manifested in the angular velocity. Extending the measurement design in [14] to include three-axis angular rate sensing as well as three-axis acceleration sensing requires a complete inertial measurement unit (IMU) for measuring the six degrees of freedom (6 dof) of a rigid body; see for example, [15]. However, the added cost and the limited dynamic range and resolution of MEMS rate gyros have motivated numerous alternative "gyro-free" IMUs for deducing the 6 dof [16–21]. The consensus is that 12 uniaxial accelerometers are required to form an overdetermined set of acceleration data for the robust reconstruction of the angular velocity of a rigid body [16,17]. Special configurations of nine [18,19] and even six [20,21] uniaxial accelerometers can also succeed. Following [17] and [21], the optimal configuration of the 6, 9, and 12 uniaxial accelerometers places them on the faces and/or the corners of a cube. The accuracy of the reconstructed angular velocity increases with cube dimension leading to dimensionally large, and thereby potentially invasive, sensor arrays. A significantly more compact solution follows from collocating angular rate gyros and accelerometers as achieved in the highly miniaturized IMU described herein.

In this paper we contribute an elegant experimental method that reveals the free-flight dynamics of a rigid body. At the heart of our method is a highly miniaturized wireless IMU that incorporates three-axis sensing of acceleration and three-axis sensing of angular velocity with a microcontroller and a low-power RF transceiver for wireless data transmission to a host computer. This IMU is used to directly measure acceleration and angular velocity during free-flight of a rigid body for comparison with theory. We directly observe the precession of the angular velocity vector in a body fixed frame through the construction of experimental polhodes. Rotations initiated close to the major, minor, and intermediate principal axes closely obey predictions from classical theory. This experimental verification of classical free-flight dynamics enables us to demonstrate that the angular velocity vector of a body in force- and torque-free flight can be reconstructed via measurements from a single, triaxial accelerometer. This simplification, which provides an inexpensive alternative to using angular rate gyros, runs counter to prior claims that a minimum of six independent accelerometer outputs are required for this purpose [20,21]. We open next with a description of the wireless IMU and the experimental procedure.

2 Methods

2.1 Wireless IMU and Experimental Procedure. Figure 1 illustrates what is believed to be the world's smallest wireless IMU enabling peer-to-peer communication to a host computer. This single-board design follows a lineage of larger, multiboard IMU designs [22–25] developed recently for novel sports training systems [26].

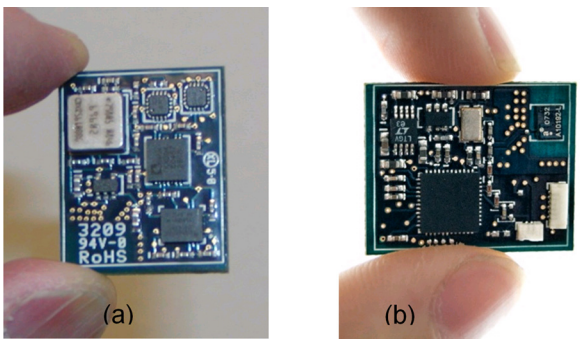

Fig. 1 Photographs of highly miniaturized, wireless IMU. (*a*) Analog circuit side with MEMS angular rate gyros and accelerometer. (*b*) Digital circuit side with microprocessor, wireless transceiver, surface mount antenna, and connectors for battery power and firmware programming.

The two faces of the design separate analog and digital circuits. The MEMS inertial sensors, mounted on the analog circuit side [Fig. 1(*a*)], include a three-axis accelerometer, one dual-axis, and one single-axis angular rate gyro, op-amps for signal conditioning, and off-chip components for filtering. The digital circuit side [Fig. 1(*b*)] includes a microprocessor for AD conversion, a low power RF transceiver, and a small surface mount antenna. Also visible are two small connectors (white, lower right) that provide battery connection and the (one-time) connection to a host computer for uploading the firmware program to the microprocessor.

The minimized footprint (0.019×0.024 m) is achieved using a six-layer board containing two internal planes for interconnects and separate planes for power and ground. The assembled IMU board has a mass of 0.003 kg and the associated miniature lithium-ion battery adds a mere 0.0015 kg. The power draw remains below 25 mW and the battery tank yields 4 h of uninterrupted use between recharging. The microprocessor performs 12-bit A/D conversion and, with the current firmware, provides 1 kHz sampling of all sensor channels. The low power RF transceiver (Nordic nRF24LE1) uses a proprietary RF protocol to transmit over a typical open-air range of 5 m with up to 18 m being achieved in low ambient RF environments. A USB-enabled receiver (not shown) enables data collection on a host (laptop) computer via custom data collection software. The device measurement range (and noise floor) includes accelerations up to 18 g ($0.1\ \text{mg}/\sqrt{\text{Hz}}$) and angular rates up to 2000 deg/s ($0.06\ \text{deg s}^{-1}/\sqrt{\text{Hz}}$) with an overall measurement bandwidth of 400 Hz. The calibration procedure detailed in [22] is used to determine 24 calibration parameters (including scale factors, cross-axis sensitivity scale factors, and biases) for the IMU. This process ensures that the acceleration and angular rate measurements are resolved along a common set of orthogonal sense axes.

This miniaturized IMU, which currently supports a wide range of human movement studies at the University of Michigan (e.g., athlete training, gait analysis, vestibular ocular reflex, knee and elbow injury detection, and surgeon training), is used herein to experimentally analyze the dynamics of a rigid body during free-flight. This class of motions is especially meaningful in the context of sports equipment (e.g., basketballs, baseballs, footballs, soccer balls, softballs, and the like) as well as aircraft, spacecraft, and smart munitions, among other applications. The IMU above enables the direct measurement of rigid-body dynamics in a non-invasive (wireless) mode in laboratory or even classroom settings.

In our experiments, we seek to measure the rotational dynamics of the example rigid body illustrated in Fig. 2. This body is a

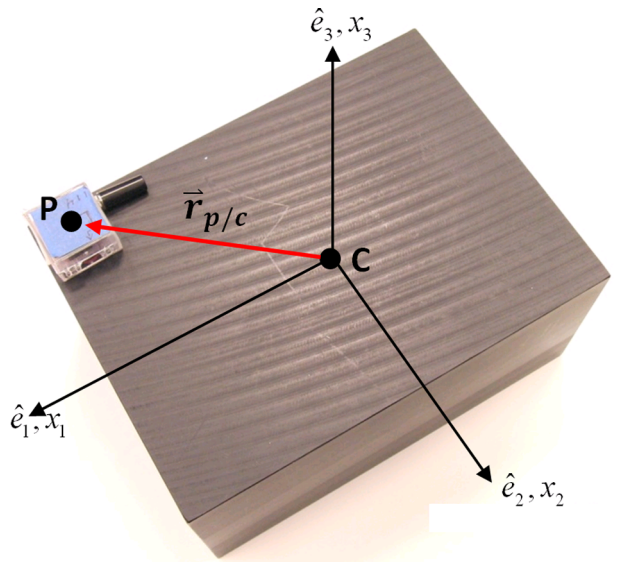

Fig. 2 Photograph of example rigid body employed in experiments

uniform block of plastic (Delrin™) having dimensions $0.201 \times 0.147 \times 0.102$ m and a mass of 4.36 kg. The block has readily computed (nondegenerate) principal moments of inertia. The miniature IMU is fastened to the surface of the block in a corner position as shown. The mass of the IMU, when enclosed in a protective plastic casing, is approximately 0.014 kg, which represents a mere 0.3% perturbation to the mass of the block. Within this casing, the MEMS accelerometer is positioned at point P which is located by the known position vector $\vec{r}_{p/c}$ relative to the mass center C of the block. The illustrated body fixed frame $(\hat{e}_1, \hat{e}_2, \hat{e}_3)$, located at C, is aligned with the principal axes of the block as well as the sense axes of the accelerometer and angular rate gyros of the IMU. In particular, the $\hat{e}_1$ axis (or x_1 axis), the $\hat{e}_2$ axis (or x_2 axis), and the $\hat{e}_3$ axis (or x_3 axis) is aligned with the minor, intermediate, and major principal axes, respectively.

A simple experimental procedure is used to record the rigid body dynamics of the block during free flight. We first select the data sampling time (typically 5 s) via a custom data collection application. Next, we initiate data collection and then launch the block into free-flight by hand. In particular, we spin the block largely about a preselected axis prior to releasing it into free-flight. The IMU wirelessly transmits the acceleration data (for point P) and the block angular velocity data before release, during free-flight, and shortly after free-flight when the block is subsequently caught by hand.

2.2 Classical Analysis of Rigid Body Rotation During Free-Flight. As our interest lies in measuring rigid body rotation during free-flight, it is instructive to quickly review the classical behaviors predicted by theory. Assuming negligible aerodynamic moments, the angular momentum of the block about its center of mass remains constant as governed by Euler's equations under torque-free conditions [4]:

$$0 = I_C \dot{\vec{\omega}} + \vec{\omega} \times I_C \vec{\omega} \tag{1}$$

Here I_C denotes the inertia tensor of the block about principal axes through its center of mass, and $\vec{\omega}$ denotes the angular velocity of the block resolved into components along the same (body-fixed) axes. Two constants of the motion arise (under the assumed torque-free conditions), namely the rotational kinetic energy (T) and the magnitude of the angular momentum ($\|\vec{H}\|$) [4] as given by

$$2T = \vec{\omega} \cdot \vec{H} = I_1 \omega_1^2 + I_2 \omega_2^2 + I_3 \omega_3^2 = \text{const.} \tag{2}$$

$$H^2 = \left\|\vec{H}\right\|^2 = (I_1\omega_1)^2 + (I_2\omega_2)^2 + (I_3\omega_3)^2 = \text{const.} \tag{3}$$

where $I_i$and ω_i (for $i = 1, 2, 3$) denote the principal moments of inertia and the angular velocity components, respectively.

The form of the solution to Eq. (1), as summarized in Table 1, depends on the intermediate principal moment of inertia I_2 and the constants of the motion T and H; see for example [27] or [28]. In Table 1, additional constants are defined by

$$z_1 = \frac{H^2 - 2T(I_2 + I_3)}{I_2 I_3}, \quad z_2 = \frac{H^2 - 2T(I_1 + I_3)}{I_1 I_3}, \quad z_3 = \frac{H^2 - 2T(I_1 + I_2)}{I_1 I_2}, \quad s_i = \text{sign}[\omega_i(0)] \tag{4}$$

and cn, sn, and dn denote Jacobi elliptic functions. The constant t_0 is evaluated by satisfying the initial conditions for $\omega(0)$.

In general, the rigid body will precess during free-flight and the precession is stable for rotations initiated close to the major and minor axes and unstable for rotations initiated close to the intermediate axis. The precession and stability can also be observed geometrically using Poinsot's construction; see for example, [1–3]. Following the development in [5], recasting the constants of the motion defined in Eqs. (2) and (3):

$$\frac{\omega_3^2}{(2T/I_3)} + \frac{\omega_2^2}{(2T/I_2)} + \frac{\omega_1^2}{(2T/I_1)} = 1 \tag{5}$$

$$\frac{\omega_3^2}{(H/I_3)^2} + \frac{\omega_2^2}{(H/I_2)^2} + \frac{\omega_1^2}{(H/I_1)^2} = 1 \tag{6}$$

yields two ellipsoidal surfaces on which the solution evolves in the space of the angular velocity components. The curve defined by their intersection is the path traced by the angular velocity vector in this space. As mentioned earlier, this curve is the polhode and it can be readily constructed directly from the IMU data as demonstrated in the following results.

3 Results and Discussion

We open our discussion with a quantitative comparison of predicted versus measured free-flight dynamics. We compare experimental and theoretical time histories of the angular velocity components as well as their companion polhodes. We then turn attention to a much simplified design employing solely a single, triaxial accelerometer in lieu of a complete IMU. In so doing, we demonstrate a new and accurate method to reconstruct the angular velocity of a rigid body in free-flight. We accomplish this by first presenting the measurement theory and then by comparing experimental predictions of angular velocity from the accelerometer to those obtained via the complete IMU.

3.1 Comparison of Experimental Versus Predicted Rigid Body Rotation. As introduced in Sec. 2, the miniature wireless IMU enables the direct sensing of rigid body rotation and thereby the direct confirmation of classical rigid body behaviors. Figure 3 illustrates typical experimental data recorded for one trial. Figures 3(*a*) and 3(*b*) illustrate the magnitude of the acceleration of point P and the magnitude of the angular velocity, respectively, as functions of time. Three distinct phases of the motion are clearly identifiable and they are referred to as the *throw*, *free-flight*, and *catch* phases. The block is spun up from rest during the throw, released into free-flight at the transition between the throw and free-flight,

Table 1 Closed-form solution to Euler's equation (1) as determined by the constants of the motion *H* and *T*

$H^2/2T > I_2$	$H^2/2T < I_2$	$H^2/2T = I_2$
$p = \sqrt{z_1 - z_2}\; k = \sqrt{z_3 - z_2}p^{-1}$	$p = \sqrt{z_3 - z_2}\; k = \sqrt{z_1 - z_2}p^{-1}$	$p = \sqrt{z_1 - z_2}$
$\omega_1 = s_1\sqrt{\frac{H^2 - 2T \cdot I_3}{I_1(I_1 - I_3)}}\text{dn}[p(t - t_0), k]$	$\omega_1 = s_1\sqrt{\frac{H^2 - 2T \cdot I_3}{I_1(I_1 - I_3)}}\text{cn}[p(t - t_0), k]$	$\omega_1 = s_1\sqrt{\frac{2T(I_2 - I_3)}{I_1(I_1 - I_3)}}\text{csc}\, h[p(t - t_0)]$
$\omega_2 = s_2\sqrt{\frac{H^2 - 2T \cdot I_1}{I_2(I_2 - I_1)}}\text{sn}[p(t - t_0), k]$	$\omega_2 = s_2\sqrt{\frac{H^2 - 2T \cdot I_3}{I_2(I_2 - I_3)}}\text{sn}[p(t - t_0), k]$	$\omega_2 = s_2\sqrt{\frac{2T}{I_2}}\tanh[p(t - t_0)]$
$\omega_3 = s_3\sqrt{\frac{H^2 - 2T \cdot I_1}{I_3(I_3 - I_1)}}\text{cn}[p(t - t_0), k]$	$\omega_3 = s_3\sqrt{\frac{H^2 - 2T \cdot I_1}{I_3(I_3 - I_1)}}\text{dn}[p(t - t_0), k]$	$\omega_3 = s_3\sqrt{\frac{2T(I_1 - I_2)}{I_3(I_1 - I_3)}}\text{csc}\, h[p(t - t_0)]$

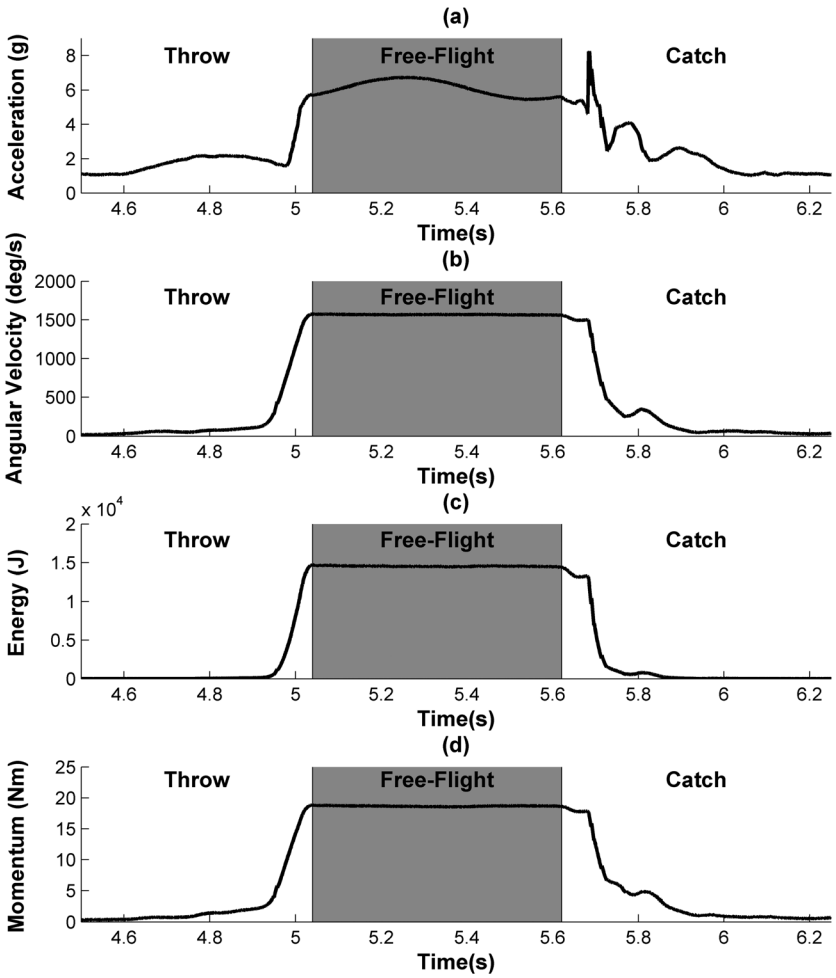

Fig. 3 Example time histories of the measured (*a*) magnitude of the acceleration of point *P*, (*b*) magnitude of the angular velocity, (*c*) the rotational kinetic energy, and (*d*) magnitude of angular momentum about center of mass. The throw, free-flight, and catch phases are noted. Example trial for rotation initiated nearly about the minor axis.

and brought back to rest during the catch. At the start of the throw, the angular velocity is zero and the magnitude of the acceleration remains 1 g[1] confirming that the block is at rest. Following a substantial spin up near the end of the throw, the magnitude of the angular velocity remains near constant (approximately 1570 deg/s) during the short (0.5 s) free-flight phase. This example trial illustrates stable rotation close to the minor axis and therefore the block exhibits a stable precession about that axis as discussed later in the context of Figs. 4 and 5. Also shown are the rotational kinetic energy T and the magnitude of the angular momentum about the center of mass $\|H\|$in Figs. 3(*c*) and 3(*d*), respectively. Note that during free-flight, T decreases by only 1.2% and $\|H\|$ decreases by a mere 0.5% confirming the negligible influence of aerodynamic moments in the experiment.

We now turn our attention to a detailed comparison of experimental and theoretical results for free-flight dynamics. Figure 4 illustrates results for rotation initiated close to the major axis [Fig. 4(*a*)], the intermediate axis [Fig. 4(*b*)], and the minor axis [Fig. 4(*c*)]. In each case, experimental (solid) and theoretical (dashed) time histories are plotted for the three angular velocity components as well as their vector magnitude (black). Recall that the components ω_1 (blue), ω_2 (green), and ω_3 (red) are aligned with the major, intermediate, and minor axes, respectively. The illustrated experimental data is low-pass filtered using a 100 Hz cut-off frequency to remove modest measurement noise. The theoretical results are computed from the solutions reported in Table 1 upon using the measured angular velocity at the start of free-flight as the initial condition for the remainder of the free-flight phase.

The results of Fig. 4 clearly confirm expected free-flight behaviors. For rotation initiated near the major (minor) axis as illustrated in Fig. 4(*a*) [Fig. 4(*c*)], the block rotates in a stable manner with a large, near-steady angular velocity component about the major (minor) axis. Moreover, the two "off-axis" components of angular velocity remain small and exhibit small periodic oscillations. The oscillation frequencies match those predicted by linear theory[2] to within 0.8% (8.3%) for the illustrated case of rotation about the major (minor) axis. In contrast, for rotation initiated near the intermediate axis as illustrated in Figs. 4(*b*), the block experiences unstable rotation as evidenced by the large, diverging precession.

The stable and unstable rotations are elegantly described geometrically upon construction of the associated polhodes as illustrated in Fig. 5. Shown in this figure are the ellipsoids of constant rotational kinetic energy (dark gray surface) and constant angular momentum

[1]Note that the MEMS accelerometer detects acceleration down to DC and thus it also measures gravity.

[2]For example, refer to [4]. This classical analysis reveals that the "off-axis" components of angular velocity will oscillate with frequency $\omega_n = \Omega\sqrt{(I_1 - I_3)(I_2 - I_1)/I_3 I_2}$ or $\omega_n = \Omega\sqrt{(I_1 - I_3)(I_3 - I_2)/I_1 I_2}$ for rotations about the major and minor axes, respectively, where Ω is the magnitude of angular velocity component about the major or minor axis.

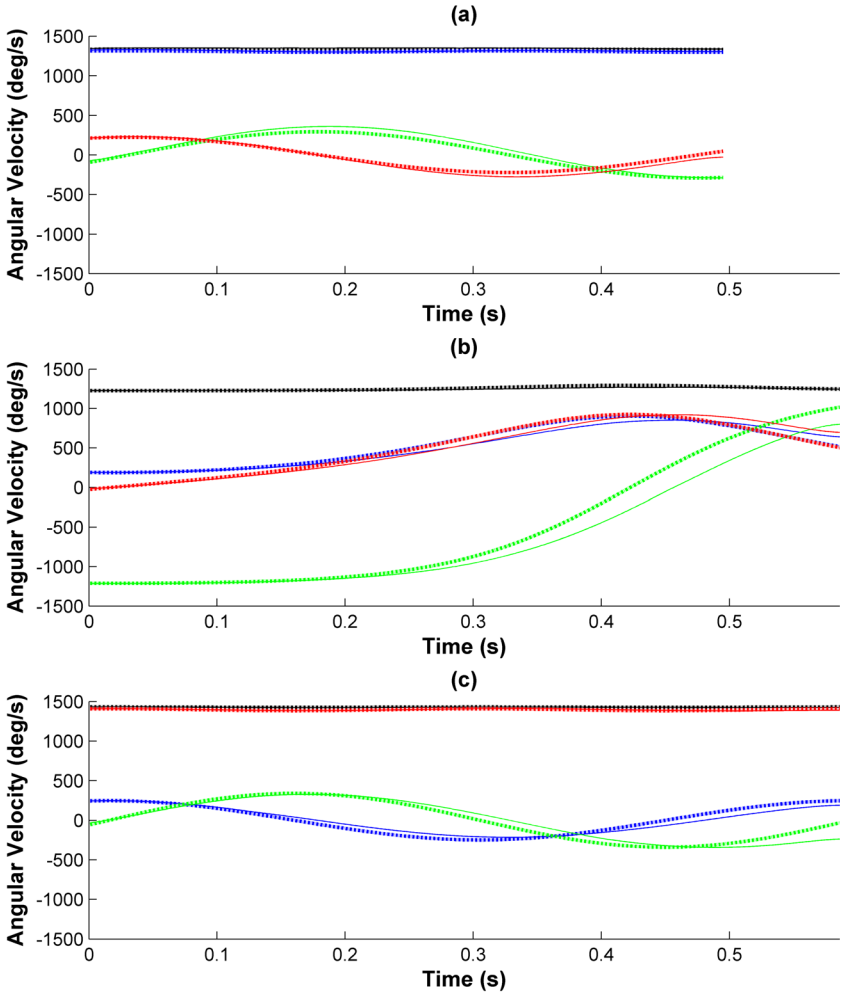

Fig. 4 Measured (solid) and calculated (dashed) angular velocity vector magnitude (black) and components for rotations initiated about the (*a*) major, (*b*) intermediate, and (*c*) minor axes. The blue, green, and red curves correspond to components about the major (ω_1), intermediate (ω_2), and minor axes (ω_3), respectively.

magnitude (light gray surface) for the case of rotation initiated near the major axis [Fig. 5(*a*)], the intermediate axis [Fig. 5(*b*)], and the minor axis [Fig. 5(*c*)]. These ellipsoids follow from Eqs. (5) and (6) upon using the measured angular velocity at the start of free-flight as the initial conditions. Following [5], the intersection of the two ellipsoids defines the curve in angular velocity space on which the free-flight dynamics evolve. This fact is confirmed upon superimposing the measured angular velocity from the wireless IMU (black curves) over the duration of the free-flight phase. For rotations initiated close to either the major or the minor axis, small-amplitude periodic precession arises and the angular velocity vector correspondingly generates a stable orbit centered about the associated principal axis; refer to Fig. 5(*a*) and 5(*c*). In contrast, for rotation initiated near the intermediate axis, the precession describes a large and diverging (unstable) response. These results provide clear and direct support of the classical theory reviewed above.

We now establish the quantitative agreement between theory and experiment. To this end, we introduce a relative error measure for each angular velocity component ω_j,

$$\varepsilon_{\mathrm{rms},j} = \sqrt{\frac{1/N\sum_{i=1}^{N}\left(\omega_{ji}-\tilde{\omega}_{ji}\right)^2}{1/N\sum_{i=1}^{N}\left\|\vec{\omega}_i\right\|^2}} \tag{7}$$

This relative error represents the root mean square error between the measured ($\tilde{\omega}_j$) and theoretical (ω_j) angular velocity components normalized by the theoretical root mean square angular velocity magnitude ($\|\vec{\omega}\|$) for all (N) samples during the free-flight phase. The theoretical angular velocity was again computed using the solutions of Table 1 upon first introducing the initial angular velocity measured by the IMU at the start of the free-flight phase. This error analysis was conducted for a total of 16 trials. The trials included two clockwise and two counterclockwise rotations about each of the three principal axis and four additional rotations about arbitrarily selected axes. The relative error, defined in Eq. (7), was calculated for each angular velocity component for each trial, and the average for all 16 trials is reported in Table 2 as a percentage.

Reflecting on the results of Table 2 and the three example trials of Fig. 4, we now understand that the wireless IMU replicates the expected theoretical angular velocity components to within 6% on average for all 16 trials. This good quantitative agreement confirms that any experimental errors introduced in the measured block inertia (i.e., m, I_1, I_2, I_3), in the IMU measurements (e.g., gyro bias, noise, calibration errors, and misalignment between sense axes and the block's principal axes), and in the assumption of torque-free motion (i.e., negligible aerodynamic moments) are reasonably small.

3.2 Angular Velocity Reconstructed From a Single Triaxial Accelerometer. The data reported above was obtained using the complete IMU including the angular rate gyros. While the angular

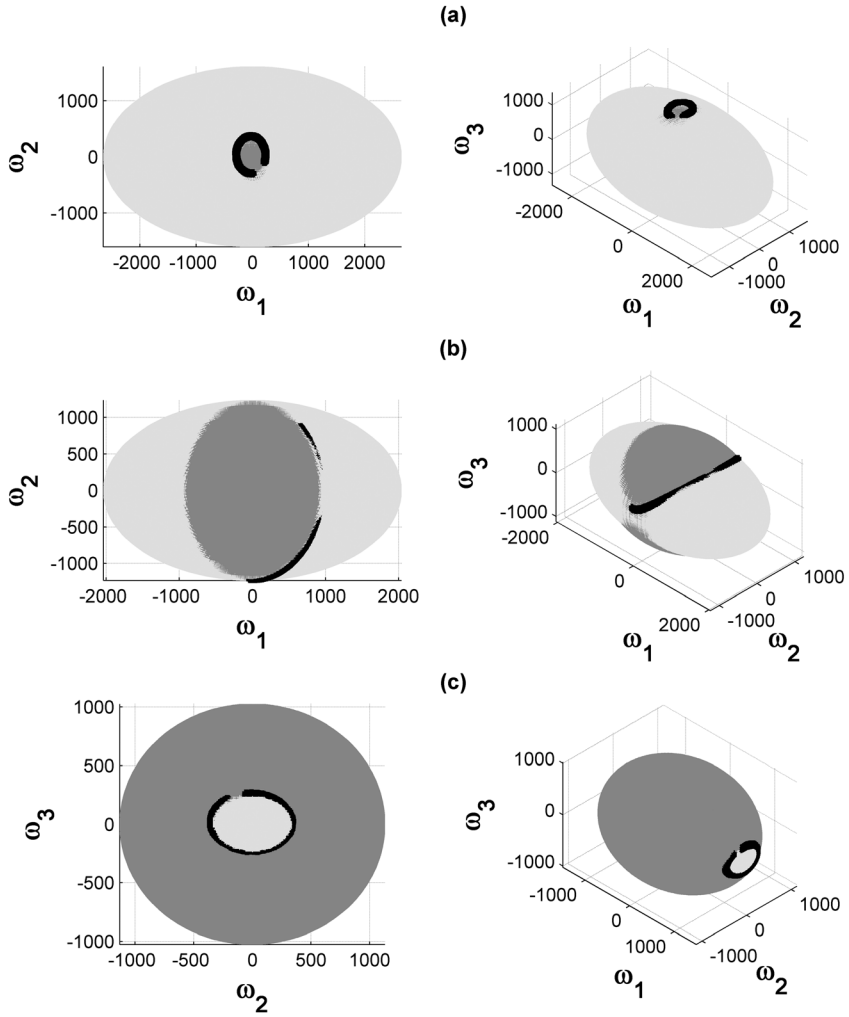

Fig. 5 Experimental demonstration of the polhode for rotations initiated close to the (*a*) major, (*b*) intermediate, and (*c*) minor principal axes. The measured angular velocity during the entire free-flight phase (black, scale in deg/s), closely follows the polhode defined by the intersection of the ellipsoids.

Table 2 Quantitative comparison of theoretical and experimental angular velocity components. Relative root-means-square error for each angular velocity component averaged over all 16 trials. The error measure is given by Eq. (7) and reported in this table as a percentage.

j	1	2	3
$\varepsilon_{\mathrm{rms},j}(\%)$	3.0	5.8	4.6

rate gyros yield highly accurate measurements of angular velocity, they are relatively expensive compared to the embedded triaxial accelerometer. The addition of angular rate gyros obviously creates a larger volume design. Moreover, commercial MEMS rate gyros have limited range (e.g., typical ranges today are 6000 deg/s and less). Thus, the restrictions incurred by rate gyro cost, size, and measurement range may preclude their use in high-volume commercial applications such as instrumented basketballs, soccer balls, baseballs, golf balls, footballs, softballs, and the like. This realization naturally leads to the question of whether it is possible to arrive at the same accurate measurements of angular velocity without the use of angular rate gyros for free-flight dynamics. We present below an answer to this question beginning with the measurement theory and then proceeding to the experimental evidence.

In reference to Fig. 2, the acceleration of point P (the center of the triaxial accelerometer) on the rigid body, can be written in terms of the acceleration of the mass center C through

$$\vec{a}_p = \vec{a}_c + \dot{\vec{\omega}} \times \vec{r}_{p/c} + \vec{\omega} \times \left(\vec{\omega} \times \vec{r}_{p/c}\right) \tag{8}$$

where $\vec{a}_c$ denotes the acceleration of the mass center, $\vec{r}_{p/c}$ is again the position of P relative to C, and $\vec{\omega}$ and $\dot{\vec{\omega}}$ are, respectively, the angular velocity and angular acceleration of the rigid body. The acceleration measured by the MEMS accelerometer is the vector sum of the acceleration of point P minus the acceleration due to gravity [20] as given by

$$\vec{a}_s = \vec{a}_p + g\hat{K} \tag{9}$$

where g denotes gravity and $\hat{K}$ is a unit vector directed upwards. For the case of a rigid body in free-flight, the acceleration of the mass center is simply

$$\vec{a}_c = -g\hat{K} \tag{10}$$

assuming negligible aerodynamic drag. Substitution of Eqs. (9) and (10) into Eq. (8) yields

$$\vec{a}_s = \dot{\vec{\omega}} \times \vec{r}_{p/c} + \vec{\omega} \times \left(\vec{\omega} \times \vec{r}_{p/c}\right) \tag{11}$$

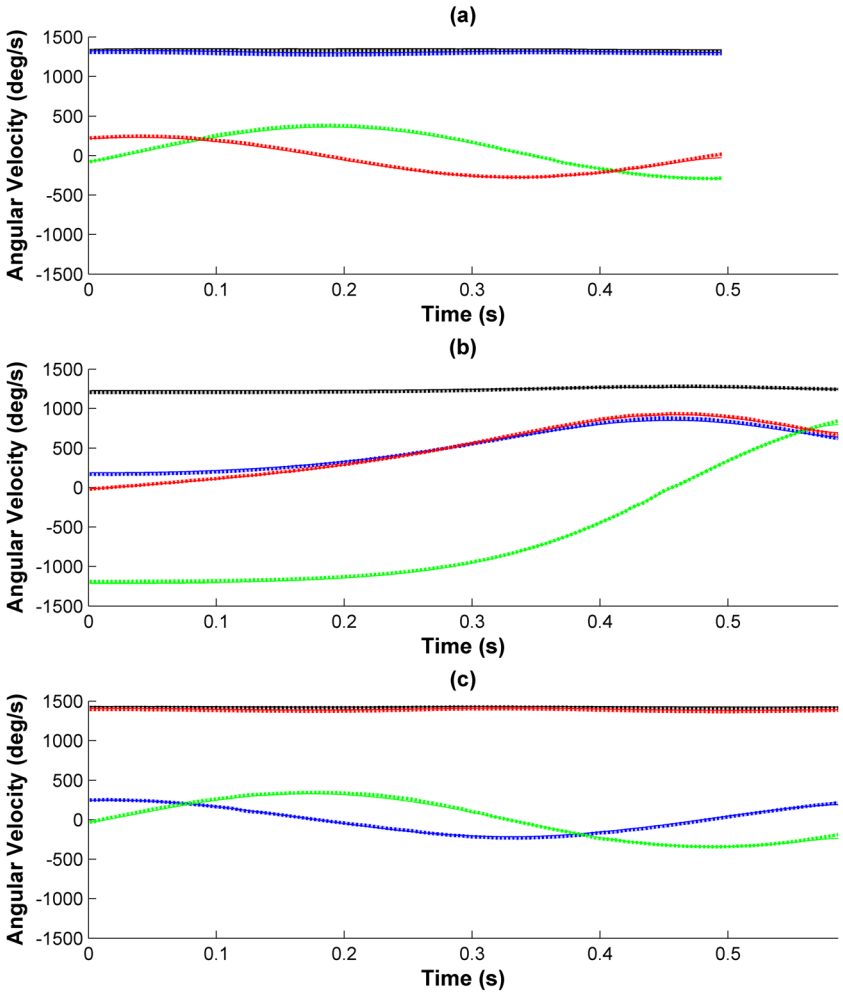

Fig. 6 Measured (solid) and reconstructed (dashed) angular velocity magnitude (black) and components for rotations initiated nearly about the (*a*) major, (*b*) intermediate, and (*c*) minor axes. The blue, green, and red curves correspond to components about the major (ω_1), intermediate (ω_2), and minor axes (ω_3), respectively.

Table 3 Relative root-mean-square error for angular velocity components reconstructed using a single, triaxial accelerometer as compared to those measured directly from the angular rate gyros

j	1	2	3
$\varepsilon_{\mathrm{rms},j}(\%)$	1.3	1.2	1.2

where it is obvious that the accelerometer output depends on the rotational dynamics of the rigid body as governed by the torque-free form of Euler's equations. Solving Eq. (1) for $\dot{\vec{\omega}}$ and substituting this result into Eq. (11) yields

$$\vec{a}_s = \left[-I_c^{-1}\left(\vec{\omega}\times I_c\vec{\omega}\right)\right]\times\vec{r}_{p/c} + \vec{\omega}\times\left(\vec{\omega}\times\vec{r}_{p/c}\right) \tag{12}$$

which explicitly demonstrates that the output of the accelerometer alone can be used to deduce the angular velocity. Introducing the components $\vec{a}_s = [\,a_{s1}\quad a_{s2}\quad a_{s3}\,]^T$ and $\vec{r}_{p/c} = [\,r_1\quad r_2\quad r_3\,]^T$ into Eq. (12) yields the component equivalent

$$\begin{bmatrix} a_{s1}\\ a_{s2}\\ a_{s3}\end{bmatrix} = \begin{bmatrix} -\left(\omega_2^2+\omega_3^2\right) & (1-I_c)\omega_1\omega_2 & (1+I_b)\omega_1\omega_3\\ (1+I_c)\omega_1\omega_2 & -\left(\omega_1^2+\omega_3^2\right) & (1-I_a)\omega_3\omega_2\\ (1-I_b)\omega_1\omega_3 & (1+I_a)\omega_3\omega_2 & -\left(\omega_1^2+\omega_2^2\right)\end{bmatrix}\begin{bmatrix} r_1\\ r_2\\ r_3\end{bmatrix} \tag{13a}$$

or

$$\vec{a}_s = \underline{B}\left(\vec{\omega}\right)\vec{r}_{p/c} \tag{13b}$$

in which $I_a = (I_2 - I_3)/I_1$, $I_b = (I_3 - I_1)/I_2$, and $I_c = (I_1 - I_2)/I_3$. Equation (13) provides three quadratic equations for solution of the three unknown angular velocity components from the measured acceleration components of point P.

Moreover, the solution for $\vec{\omega}$ must satisfy the two constants of the motion given by Eqs. (2) and (3). These additional equations, though not independent of the above result that embeds Euler's equations, are advantageous in the computation of $\vec{\omega}$. In particular, Eq. (13) with Eqs. (2) and (3) yield an overdetermined set of five equations in the three unknowns $(\omega_1, \omega_2, \omega_3)$ enabling a robust least squares solution, provided the values of the constants of the motion are known a priori.

To compute these constants, we first seek the initial conditions for the angular velocity and the two constants of the motion as represented by the set $[\omega_1(0), \omega_2(0), \omega_3(0), 2T_0, H_0^2]$. To this end, we numerically solve Eq. (13) with Eqs. (2) and (3) as a set of five equations in these five unknowns using the measured values of $[a_{s1}(0), a_{s2}(0), a_{s3}(0)]$ at the start of the free-flight phase. This set of nonlinear equations admits multiple solutions which is a well documented issue; see for example [16,19,20,29,30]. The problem, illustrated by Eq. (11), is that the expression for $\vec{a}_s$ is quadratic in $\vec{\omega}$ which renders the sign of the angular velocity vector

(though not the direction) ambiguous. The sign can be readily determined by simple observation during the experiment.

For any other time t during the free-flight phase, we compute the least-squares solution for $\vec{\omega}(t)$ from the five equations (13) with (2) and (3). For each sample i, we seek the solution for $\vec{\omega}$ that minimizes the cost function

$$J_i = \left(\frac{\left\| \vec{a}_{s,i} - \underline{B}\left(\vec{\omega}\right)\vec{r}_{p/c} \right\|}{\sum_{i=1}^{N} \left\| \vec{a}_{s,i} \right\| / N} \right)^2 + \left(\frac{2T_0 - 2T_i}{2T_0} \right)^2 + \left(\frac{H_0^2 - \left\| \vec{H}_i \right\|^2}{H_0^2} \right)^2 \tag{14}$$

where $\vec{a}_{s,i}$ is the sampled accelerometer output, and N is the total number of samples. The solution is found numerically using the *lsqnonlin* function in MATLAB ™ and angular velocity components from the last time step as an initial guess. The *lsqnonlin* function employs a trust-region method for numerical, unconstrained, nonlinear, minimization problems [31].

The components of angular velocity, as reconstructed from a single triaxial accelerometer, reliably predict those measured by the angular rate gyros. Evidence for this claim is presented in Fig. 6 which directly compares the reconstructed versus measured angular velocity. Results are presented for three example trials where rotation is initiated nearly about the major [Fig. 6(*a*)], the intermediate [Fig. 6(*b*)], and the minor [Fig. 6(*c*)] axes. Both the angular velocity components as well as the magnitude of the angular velocity vector are illustrated. Inspection of these results reveals excellent agreement thereby demonstrating that a single, triaxial accelerometer can be employed to accurately reconstruct the angular velocity during free-flight. The accuracy is summarized quantitatively in Table 3 which reports the average relative rms error[3] for the 16 trials previously considered. The errors, which remain less than 2% for all three angular velocity components, provide convincing evidence in support of our claim.

4 Summary and Conclusions

The novel, miniature wireless MEMS IMU presented herein provides a noninvasive and highly portable means to measure the dynamics of a rigid body. The IMU incorporates three-axis sensing of acceleration and three-axis sensing of angular velocity with a microcontroller and an RF transceiver for wireless data transmission to a host computer. The small sensor footprint (0.019×0.024 m) and mass (0.005 kg including battery) enables its use in rather broad applications including; for example, human motion analysis, sports training systems, and education/learning of rigid body dynamics. Specific to this paper, we demonstrate how this novel sensor can be used in laboratory or classroom settings to accurately measure the dynamics of a rigid body in free-flight.

The experiments consider an example rigid body that is spun up by hand and then released into free-flight. The resulting rotational dynamics measured by the angular rate gyros are carefully benchmarked against theoretical results from Euler's equations. This comparison reveals that differences between measurement and theory remain less than 6%. Moreover, experimentally constructed polhodes elegantly illustrate the expected stable precession for rotations initiated close to the major or minor principal axes and the unstable precession for rotations initiated close to the intermediate axis.

Finally, we present a single, triaxial accelerometer as an alternative to using a full IMU for deducing the angular velocity of a rigid body during free-flight. This simpler alternative, which addresses restrictions incurred by rate gyro cost, size, and measurement range, may enable high-volume commercial applications such as instrumented basketballs, soccer balls, baseballs, golf balls, footballs, softballs, and the like. A measurement theory is presented for reconstructing the angular velocity of the body during free-flight from acceleration signals which is then validated experimentally. The experimental results confirm that the angular velocity can be reconstructed with small errors (less than 2%) when benchmarked against direct measurements using angular rate gyros.

[3]The error measure is again given by (7) where the angular velocity measured by the angular rate gyros is now used as the "truth" data.

Acknowledgment

The authors gratefully acknowledge past support from the University of Michigan Graduate Medical Education Innovations Fund and from Ebonite International for the development of the wireless IMU. The first author also gratefully acknowledges support provided by a National Science Foundation Graduate Student Fellowship.

References

[1] Routh, E. J., 1860, *Dynamics of a System of Rigid Bodies*, 6th ed., MacMillan, New York.
[2] Gray, A., 1918, *Treatise on Gyrostatics and Rotational Motion*, MacMillan, London.
[3] Goldstein, H., 1922, *Classical Mechanics,* 2nd ed., Addison-Wesley, Reading, MA.
[4] Greenwood, D. T., 1988, *Principles of Dynamics*, Prentice-Hall, Englewood Cliffs, NJ.
[5] Wie, B., 1998, *Space Vehicle Dynamics and Control*, American Institute of Aeronautics and Astronautics, Reston, VA.
[6] Mettler, B. F., 2010, "Extracting Micro Air Vehicles Aerodynamic Forces and Coefficients in Free Flight Using Visual Motion Tracking Techniques," Exp. Fluid Mech., **49**, pp. 577–569.
[7] Aghili, F., and Parsa, K., 2009, "Motion and Parameter Estimation of Space Objects Using Laser Vision Data," J. Guidance Control Dyn., **32**(2), pp. 537–549.
[8] Lichter, M. D., and Dubowsky, S., 2004, "State, Shape, and Parameter Estimation of Space Objects from Range Images," Proceedings of the 2004 IEEE International Conference on Robotics & Automation, New Orleans, LA, pp. 2974–2979.
[9] Hillenbrand, U., and Lampariello, R., 2005, "Motion and Parameter Estimation of a Free-Floating Space Object from Range Data for Motion Prediction," 8th International Symposium on Artificial Intelligence, Robotics, and Automation in Space.
[10] Kim, S.-G., Crassidis, J. L. Cheng, Y. Fosbury, A. M., and Junkins, J. L., 2007, "Kalman Filtering for Relative Spacecraft Attitude and Position Estimation," J. Guidance Control Dyn., **30**(1), pp. 133–143.
[11] Thienel, J. K., and Sanner, R. M., 2007, "Hubble Space Telescope Angular Velocity Estimation During the Robotic Servicing Mission," J. Guidance Control Dyn., **30**(1), pp. 29–34.
[12] Bhat, K. S., Seitz, S. M., Popovic, J., and Khosla, P. K., 2002, "Computing the Physical Parameters of Rigid-Body Motion from Video," Lecture Notes in Computer Science, **2350**, pp. 551–565.
[13] Masutani, Y., Iwatsu, T., and Miyazaki, F., 1994, "Motion Estimation of Unknown Rigid Body Under No External Forces and Moments," Proceedings of IEEE International Conference on Robotics and Automation 1994, IEEE Computer Society Press, New York, Vol. 2, pp. 1066–1072.
[14] Lorenz, R. D., 2005, "Flight and Attitude Dynamics Measurements of an Instrumented Frisbee," Meas. Sci. Technol., **16**, pp. 738–748.
[15] Titterton, D., and Weston, J., 2004, *Strapdown Inertial Navigation Technology*, 2nd ed., The Institution of Electrical Engineers, Stevenage, Herts, UK.
[16] Zappa, B., Legnani, G., van den Bogert, A., and Adamini, R., 2001, "On the Number and Placement of Accelerometers for Angular Velocity and Acceleration Determination," ASME J. Dyn. Syst. Meas. Control, **123**, pp. 552–554.
[17] Cardou, P., and Angeles, J., 2008, "Angular Velocity Estimation From the Angular Acceleration Matrix," ASME J. Appl. Mech., **75**(2), p. 021003.
[18] Mital, N. K., and King, A. I., 1979, "Computation of Rigid-Body Rotation in Three-Dimensional Space from Body-Fixed Linear Acceleration Measurements," ASME J. Appl. Mech., **46**, pp. 925–930.
[19] Genin, J., Hong, J., and Xu, W., 1997, "Accelerometer Placement for Angular Velocity Determination," ASME J. Dyn. Syst. Meas. Control, **119**(3), pp. 474–477.
[20] Chen, J., Lee, S., and DeBra, D. B., 1994, "Gyroscope Free Strapdown Inertial Measurement Unit by Six Linear Accelerometers," J. Guidance Control Dyn., **17**(2), pp. 286–290.
[21] Hanson, R., and Pachter, M., 2005, "Optimal Gyro-Free IMU Geometry," AIAA Guidance, Navigation, and Control Conference and Exhibit 15–18 August 2005, San Francisco, CA.
[22] King, K. W., 2008, "The Design and Application of Wireless MEMS Inertial Measurement Units for the Measurement and Analysis of Golf Swings," Ph.D. Thesis, University of Michigan, Ann Arbor, MI.
[23] King, K. W., and Perkins, N. C., 2008, "Putting Stroke Analysis Using MEMS Inertial Sensor Systems," World Scientific Congress on Golf V, Phoenix, AZ, pp. 270–278.

[24] King, K. W., Yoon, S. W., Perkins, N. C., and Najafi, K., 2004, "The Dynamics of the Golf Swing as Measured by Strapdown Inertial Sensors," Proceedings 5th International Conference on the Engineering of Sport, Davis, CA, pp. 276–282.
[25] King, K. W., Yoon, S. W., Perkins, N. C., and Najafi, K., 2008, "Wireless MEMS Inertial Sensor System for Golf Swing Dynamics," Sensors Actuators A, **141**(2), pp. 619–630.
[26] Perkins, N. C., 2007 and 2006, "Electronic Measurement of the Motion of a Moving Body of Sports Equipment," US Patent Numbers 7,234,351 and 7,021,140.
[27] Kane, T. R., Likins, P. W., and Levinson, D. A., 1983, *Spacecraft Dynamics*, McGraw-Hill, New York.
[28] van Zon, R., and Schofield, J., 2007, "Numerical Implementation of the Exact Dynamics of Free Rigid Bodies," J. Comput. Phys., **225**(1), pp. 145–164.
[29] Williams, T., Pahadia, A., Petovello, M., and Lachapelle, G., 2009, "Using an Accelerometer Configuration to Improve the Performance of a MEMS IMU: Feasibility Study With a Pedestrian Navigation Application," ION GNSS 2009, Session F4, Savannah, GA.
[30] Ciblak, N., 2007, "Determining the Angular Motion of a Rigid Body Using Linear Accelerometers Without Integration," 3rd International Conference on Recent Advances in Space Technologies. RAST '07, pp. 585–590.
[31] Moré, J. J., and Sorensen, D. C., 1983, "Computing a Trust Region Step," SIAM J Sci. Comput., **4**(3), pp. 553–572.